

# Collective Excitations of Self-Gravitating Bose-Einstein Condensates: Breathing Mode and Appearance of Anisotropy under Self-Gravity

Kenta Asakawa<sup>1,\*</sup>, Hideki Ishihara<sup>1,2,†</sup> and Makoto Tsubota<sup>1,2,‡</sup>

<sup>1</sup> *Department of Physics, Osaka Metropolitan University,  
3-3-138 Sugimoto, Sumiyoshi-Ku, Osaka 558-8585,*

*Japan* <sup>2</sup> *Nambu Yoichiro Institute of Theoretical and Experimental Physics (NITEP),  
Osaka Metropolitan University, 3-3-138 Sugimoto, Sumiyoshi-Ku, Osaka 558-8585, Japan*

(Dated: November 30, 2023)

We study the collective mode of self-gravitating Bose-Einstein condensates (BECs) described by the Gross-Pitaevskii-Poisson (GPP) equations. The self-gravitating BEC recently receives significant attention in cosmology and astrophysics as a candidate for dark matter. We investigate the breathing and anisotropic collective modes by numerically solving the GPP equations and using the variational method. The breathing mode shows that the period decreases with the total mass due to the density dependence of the self-gravitating BEC, which is quantitatively consistent with our analytical results. We also obtain an anisotropic collective mode, in which the quadrupole mode is coupled with the breathing mode. The period of the quadrupole mode has the same total mass dependence as that of the breathing mode. The characteristics of these periods are different from those of ordinary BECs trapped by an external potential. However, despite the difference in density dependence, the ratio of their periods is equal to that of the BEC trapped by an isotropic harmonic potential. Furthermore, a variational method extended to a spheroidal configuration shows that we extract only the quadrupole mode from the anisotropic collective mode.

## I. INTRODUCTION

Dark matter (DM) is one of the most important subjects in cosmology, astrophysics, and modern physics. The nature and identity have taken our attention for some decades. The characteristics of the DM is that it does not emit, reflect, or absorb light, but interact gravitationally with other matter. Although we cannot directly observe the DM by any optical way, we can find the evidences of existence from the rotational curve of galaxies [1] and gravitational lensing [2] [3].

Recently, the  $\Lambda$  cold dark matter ( $\Lambda$ CDM) model assuming the non-relativistic dark matter particles is a standard cosmological model. It succeeds in describing the large-scale structures of the universe and has been used for various cosmological and astrophysical studies [4]. However, it is also well-known that the  $\Lambda$ CDM model has serious discrepancies at small scales between the observational and theoretical results [5]. In order to resolve this, some alternate models have been proposed [6]; assuming that, for example, the ultralight scalar particles behave as the DM [7, 8] or the non-gravitational self-interaction between the DM particles [9, 10].

An attractive probability is recently discussed: a Bose-Einstein condensation of the DM halo assuming the ultralight DM by scalar particles [11–13]. A Bose-Einstein condensation is a phenomenon that the macroscopic quantity of Bose particles in a system condenses into a common quantum state. As a result, the physical state of the Bose-Einstein condensate (BEC) is written by the

macroscopic wavefunction which shows the coherence of the BEC. This phenomenon occurs when the temperature of the Bose gas is lower than the critical temperature for the Bose-Einstein condensation, which means that the de Broglie wavelength of Bose particles is larger than the mean interparticle distance [14].

A Bose-Einstein condensation of the ultralight scalar particles probably alleviate the discrepancies of the  $\Lambda$ CDM model. When the mass of the scalar particles is  $m \sim 10^{-23} - 10^{-22}$  eV, they can reproduce the large-scale structures like the  $\Lambda$ CDM model [15, 16]. Furthermore, the Bose gas shows the high critical temperature for the Bose-Einstein condensation in the order of  $10^9$  K [17] due to the galactic-scale de Broglie wavelength of the order of 1 kpc [12, 18]. Therefore, the DM halo of such ultralight scalar particles can become a BEC in the Universe. Because of the ultralight mass, scalar particles macroscopically show their quantumness in such BEC DM halo, and the uncertainty relation suppresses the overpopulation of the DM at small scales. The promising candidate of such ultralight DM is, for example, an axion-like particle proposed in the string theory [19].

A BEC of dark matter is intriguing within the realm of low temperature physics, as it posits the existence of a galaxy-scale quantum fluid beyond the confines of laboratory settings. The quantum fluid such as superfluids  $^4\text{He}$ ,  $^3\text{He}$ , and atomic BECs is defined as a fluid that the quantum effect macroscopically emerges due to the ultra-low temperature. The various studies on these fluids (e.g. the collective mode [20], the quantized vortex [21], and the quantum turbulence [22, 23]) have been conducted in low temperature physics [14, 24, 25]. Particularly, a BEC near zero temperature is quantitatively described by the Gross-Pitaevskii (GP) equation which represents the time evolution of a macroscopic wave-

\* sn22896p@st.omu.ac.jp

† h.ishihara@omu.ac.jp

‡ tsubota@omu.ac.jp

function [26, 27]. Considering a BEC of the ultralight DM, it should be bound by the gravitational potential of the BEC itself and such self-gravitating BEC follows the Gross-Pitaevskii-Poisson (GPP) equations [16, 28, 29].

The GPP equations allow the DM to introduce the short-range contact interaction. As above, such self-interaction of the DM is also suggested to resolve the discrepancies of  $\Lambda$ CDM model. The possibility that the DM has the non-negligible and non-gravitational self-interaction is suggested by some observational results of colliding clusters of galaxies [30, 31].

A self-gravitating BEC obviously differs from an atomic BEC in their trapping potential. In low temperature physics, the BEC is generally trapped by external potentials. The external potential is prescribed independently of the configuration of the BEC, regardless of how much it moves. On the other hand, a self-gravitating BEC is trapped by its own gravitational potential, even without any external potential. Then, the deformation of the self-gravitating BEC can change the depth, range, and anisotropy of the gravitational potential. Such differences between a self-gravitating BEC and an atomic BEC are quite important when we consider the former as a candidate for astrophysical objects because it causes quantum hydrodynamical phenomena under the self-gravity.

One of phenomena that the anisotropy of the trapping potential affects is the collective mode. It is defined as a low-frequency oscillation of a trapped BEC in response to small fluctuations. The collective mode can be described by representative variables as a one-body motion, despite being a many-body system. For example, a spherically trapped BEC can show the collective mode characterized by the radius, called monopole (breathing) mode, and that characterized by two semi-axes or the ratio of these, called quadrupole mode. One of the most important characteristics is that the collective modes depend on the shape of the trapping potential; considering the axisymmetric potential, the breathing and quadrupole modes are coupled. Because the gravitational potential of self-gravitating BECs changes with the oscillation of the BEC, the collective mode of a self-gravitating BEC is likely to exhibit a behavior different from the usual one.

Various properties of DM halos have been studied theoretically using the GPP equations in recent astrophysics studies.

The Thomas-Fermi (TF) approximation of the GP equation is useful to describe the equilibrium state of a BEC and carry out the analytical studies. As far as a self-gravitating BEC, this approximation was applied for the first time to compare the consequences with the observational data on the rotational curves of galaxies [32]. Subsequently, many studies using the approximation have appeared, including the divergence of the central density of the  $\Lambda$ CDM model called the core-cusp problem [33], gravitational lensing effects [34], deformation by rotation [35], and the effects of quantized vortices [36, 37].

A self-gravitating BEC has also been studied by the

variational method. In low temperature physics, the calculation of the collective mode of a BEC by this method is well-known and standard [14, 24]. Applying the variational method to a self-gravitating BEC, the relationship between the total mass and radius of self-gravitating BECs [28], gravitational collapse [38, 39], and the phase transition between dilute and dense phases [40] were investigated.

Numerical studies on self-gravitating BECs have recently been reported. It is extraordinarily complicated and difficult to analytically solve the GPP equations for general situations. Thus, the numerical calculation of the GPP equations is required in order to study a self-gravitating BEC. Thus far, the stability of the equilibrium state [41], the stabilization process [42], the rotational velocity of a test particle in a self-gravitating BEC [43, 44], the collision of self-gravitating BECs [45] were numerically investigated by imposing spatial symmetry on the system in order to reduce computational costs. However, latest numerical studies used a three-dimensional system without spatial symmetry; they focused on quantized vortices in self-gravitating BECs, such as the stability [46, 47] and the collision of self-gravitating BECs with quantized vortices [48].

In this work, we study the three-dimensional dynamics of the collective modes of a self-gravitating BEC. We consider the total mass to be sufficiently large that a TF approximation is available. We prepare the initial state by multiplying the factor on the initial velocity with the equilibrium solution of the GPP equations and implement time evolution by numerically solving the GPP equations. First, the breathing mode of the self-gravitating BECs is induced by radially adding the initial velocity. Our numerical results agree with the analytical results obtained using the variational method. Next, by adding the initial velocity axisymmetrically, we numerically obtain the anisotropic collective mode in which the quadrupole mode is mixed with the breathing mode.

This paper is organized as follows. Our model and numerical setup are described in Sec.II. Based on this, the breathing mode of a self-gravitating BEC is studied in Sec.III. Anisotropic collective mode under self-gravity of the BEC is investigated in Sec.IV. Finally, we conclude this paper in Sec.V.

## II. MODEL AND NUMERICAL SETUP

### A. GROSS-PITAEVSKII-POISSON MODEL AND THE EQUILIBRIUM STATE

We consider that a self-gravitating BEC consisted of scalar bosons with mass  $m$  and an s-wave scattering length  $a$  at zero temperature. In the GPP model, the physical state of the BEC is described by the macroscopic wavefunction  $\psi(\mathbf{r}, t)$  and the time evolution is given by

the GPP equations:

$$\begin{cases} i\hbar\partial_t\psi = -\frac{\hbar^2}{2m}\nabla^2\psi + [mV + \frac{4\pi\hbar^2 a}{m}|\psi|^2]\psi, \\ \nabla^2 V = 4\pi mG|\psi|^2, \end{cases} \quad (1)$$

where  $V(\mathbf{r}, t)$  denotes the gravitational potential [13, 16, 28]. Using the Madelung representation

$$\psi(\mathbf{r}, t) = \sqrt{\frac{\rho(\mathbf{r}, t)}{m}} e^{i\theta(\mathbf{r}, t)}, \quad (2)$$

the GP equation becomes the continuity equation and the Euler-like equation, where  $\rho = m|\psi|^2$  denotes the density and  $\mathbf{v} = \hbar\nabla\theta/m$  denotes the velocity field [14]. Then, the total mass is

$$M = \int d\mathbf{r} \rho(\mathbf{r}) = m \int d\mathbf{r} |\psi|^2. \quad (3)$$

The total energy  $E$  is the sum of these energies:

$$E = K + W + I, \quad (4)$$

$$K = \frac{\hbar^2}{2m} \int d\mathbf{r} |\nabla\psi|^2, \quad (5)$$

$$W = \frac{m}{2} \int d\mathbf{r} |\psi|^2 V, \quad (6)$$

$$I = \frac{2\pi\hbar^2 a}{m} \int d\mathbf{r} |\psi|^4, \quad (7)$$

where  $K$  denotes the kinetic energy,  $W$  denotes the potential energy, and  $I$  denotes the self-interaction energy [36].

We can obtain the equilibrium solution of the GPP equations (1) using the TF approximation [32]. When the kinetic energy is neglected *i.e.*,  $K \ll I$ , the configuration of the equilibrium state is formed by the competition between gravity and self-interaction [14]. The kinetic energy is negligible when the total mass is sufficiently large [49]. The equilibrium configuration should be spherically symmetrical under self-gravity. Assuming that the equilibrium state satisfies the ansatz  $\psi(\mathbf{r}, t) = \phi(r)e^{-i\mu t/\hbar}$ , the steady solution of Eq. (1) is approximately

$$\begin{aligned} \rho(r) &\simeq \rho_c j_0(\pi r/R_{\text{TF}}) \\ &= \rho_c \frac{\sin(\pi r/R_{\text{TF}})}{(\pi r/R_{\text{TF}})} \quad (r < R_{\text{TF}}), \end{aligned} \quad (8)$$

where  $r = |\mathbf{r}|$  is the radial coordinate,  $\mu$  is the chemical potential,  $\rho_c$  is the central density, and  $j_0$  is the 0-th spherical Bessel function. Subsequently, the TF radius  $R_{\text{TF}}$  is defined as the minimum radius at which the density becomes zero:

$$R_{\text{TF}} = \pi \sqrt{\frac{\hbar^2 a}{Gm^3}}, \quad (9)$$

which implies that the size of a massive self-gravitating BEC does not depend on its total mass. There are no

densities in the range of  $r > R_{\text{TF}}$ . Thus, the cumulative mass profile is

$$M(r) = \begin{cases} \frac{M_{\text{TF}}}{\pi} \left\{ \sin\left(\frac{\pi r}{R_{\text{TF}}}\right) - \frac{\pi r}{R_{\text{TF}}} \cos\left(\frac{\pi r}{R_{\text{TF}}}\right) \right\} & (r < R_{\text{TF}}), \\ M_{\text{TF}} & (r > R_{\text{TF}}), \end{cases} \quad (10)$$

where  $M_{\text{TF}}$  denotes

$$M_{\text{TF}} = \frac{4\rho_c R_{\text{TF}}^3}{\pi}. \quad (11)$$

Since the TF radius is independent of the total mass, Eq. (11) shows that only the central density increases, even when the total mass increases. By solving the Poisson equation, the gravitational potential becomes

$$\begin{aligned} V(r) &= G \int_{\infty}^r ds \frac{M(s)}{s^2} \\ &= \begin{cases} -\frac{GM_{\text{TF}}}{R_{\text{TF}}} \left\{ 1 + j_0\left(\frac{\pi r}{R_{\text{TF}}}\right) \right\} & (r < R_{\text{TF}}), \\ -\frac{GM_{\text{TF}}}{r} & (r > R_{\text{TF}}). \end{cases} \end{aligned} \quad (12)$$

Therefore, using Eqs. (5), (6), (7), (8), and (12), the energy of each equilibrium state is

$$K \simeq \frac{\pi}{8} \frac{\hbar^2 M_{\text{TF}}}{m^2 R_{\text{TF}}^2} \left\{ \text{Si}(\pi) - \pi + \int_0^{\Lambda\pi} dx \frac{x}{\sin x} \right\}, \quad (13)$$

$$W = -\frac{3}{4} \frac{GM_{\text{TF}}^2}{R_{\text{TF}}}, \quad (14)$$

$$I = \frac{\pi^2}{4} \frac{\hbar^2 a M_{\text{TF}}^2}{m^3 R_{\text{TF}}^3}, \quad (15)$$

where  $\text{Si}(x)$  is a sine integral and  $\Lambda\pi (< \pi)$  is the cutoff to avoid the divergence of the integral for  $\Lambda \rightarrow 1$ . The value of  $\Lambda$  can be estimated using the ratio between the coherence length  $\xi = \sqrt{m/(8\pi a\rho_c)}$  and the TF radius, such that  $\Lambda \sim 1 - \xi/R_{\text{TF}}$ .

## B. NUMERICAL SETUP

The GPP equations (1) are reduced to the following dimensionless form:

$$\begin{cases} i\tilde{\partial}_t \tilde{\psi} = -\frac{1}{2} \tilde{\nabla}^2 \tilde{\psi} + [\tilde{V} - i\tilde{V}_s + \tilde{a}|\tilde{\psi}|^2]\tilde{\psi}, \\ \tilde{\nabla}^2 \tilde{V} = |\tilde{\psi}|^2, \end{cases} \quad (16)$$

where the tilde symbols represent the dimensionless variables. The dimensionless variables are defined by,  $\tilde{\mathbf{r}} = \mathbf{r}(\tilde{\lambda}mc/\hbar)$ ,  $\tilde{t} = t(\tilde{\lambda}^2 mc^2/\hbar)$ ,  $\tilde{\psi} = \psi\{\sqrt{4\pi G\hbar}/(\sqrt{mc^2}\tilde{\lambda}^2)\}$ ,  $\tilde{V} = V/(\tilde{\lambda}^2 c^2)$ ,  $\tilde{a} = a\{\tilde{\lambda}^2 c^2/(mG)\}$  [43]. The scale factor  $\tilde{\lambda}$  can arrange the system size using the invariance of the equations for any value [60]. Then, the dimensionless total mass and energy are,  $\tilde{M} = M\{4\pi Gm/(\tilde{\lambda}\hbar c)\}$  and  $\tilde{E} = E\{8\pi Gm/(\hbar c^3\tilde{\lambda}^3)\}$ .

The boundary conditions should be considered when addressing Eq. (16). The GP equation is typically solved under periodic boundary conditions. However, the Poisson equation is inconsistent with the periodic boundary condition owing to the long-range interaction of gravity. To overcome this inconsistency, we propose a novel method.

The GP equation in Eq. (16) is computed using the fourth-order Runge-Kutta and pseudo-spectrum methods under periodic boundary conditions. To solve the Poisson equation, we use the finite difference and Jacobi methods at each time step [50]. Using the Jacobi method, the solution of the Poisson equation in Eq. (16) is the equilibrium solution of the diffusion equation for the function  $\tilde{V}'(\tilde{\mathbf{r}}, \tilde{t}; \tilde{s})$ :

$$\frac{d\tilde{V}'}{d\tilde{s}}(\tilde{\mathbf{r}}, \tilde{t}; \tilde{s}) = \tilde{\nabla}^2 \tilde{V}'(\tilde{\mathbf{r}}, \tilde{t}; \tilde{s}) - |\tilde{\psi}(\tilde{\mathbf{r}}, \tilde{t})|^2, \quad (17)$$

where  $\tilde{s}$  denotes a real parameter. The gravitational potential is obtained from  $\tilde{V}(\tilde{\mathbf{r}}, \tilde{t}) = \lim_{\tilde{s} \rightarrow \infty} \tilde{V}'(\tilde{\mathbf{r}}, \tilde{t}; \tilde{s})$ . Furthermore, the Jacobi method can be dramatically improved by Nesterov's accelerated gradient method [51–53]. This method is common in the field of machine learning and enables us to rapidly obtain the function  $\tilde{V}'(\tilde{\mathbf{r}}, \tilde{t}; \tilde{s})$  optimized by Eq. (17). The function  $\tilde{V}'(\tilde{\mathbf{r}}, \tilde{t}; \tilde{s})$  satisfies the Dirichlet boundary condition:

$$\tilde{V}'(\tilde{\mathbf{r}} = \tilde{\mathbf{R}}_b, \tilde{t}; \tilde{s}) = -\frac{\tilde{M}}{4\pi|\tilde{\mathbf{R}}_b - \tilde{\mathbf{R}}_c|} \quad (18)$$

where  $\tilde{\mathbf{R}}_b$  is the position on the boundary of the numerical domain and  $\tilde{\mathbf{R}}_c$  is the center of the numerical domain. The boundary condition (18) is appropriate when the BEC is smaller than the numerical domain and located near its center.

In our numerical model, the imaginary potential  $-i\tilde{V}_s$ , called "sponge" potential, such as

$$\tilde{V}_s(\mathbf{r}) = \frac{\tilde{V}_o}{2} \left\{ 2 + \tanh\left(\frac{\tilde{r} - \tilde{r}_c}{\tilde{\delta}}\right) - \tanh\left(\frac{\tilde{r}_c}{\tilde{\delta}}\right) \right\} \quad (19)$$

is introduced into Eq. (16) [43].  $\tilde{V}_o$  denotes the amplitude. This sponge potential can reduce the number of particles in the range of  $\tilde{r} > \tilde{r}_c$ , where  $\tilde{\delta}$  is the step width. The sponge potential plays a role in removing particles emitted from the BEC. When the BEC moves, some particles obtain high kinetic energy and escape from the gravitational potential. However, in our system, they return to the BEC by a periodic boundary condition for the GP equation. In order to avoid the unphysical situation, we require the sponge potential.

The initial state is prepared by multiplying the factor of the initial phase  $\exp[i\tilde{\phi}(\tilde{\mathbf{r}})]$  to the equilibrium state  $\tilde{\psi}_{\text{eq}}(\tilde{\mathbf{r}})$ :

$$\tilde{\psi}(\tilde{\mathbf{r}}, \tilde{t} = 0) = \tilde{\psi}_{\text{eq}}(\tilde{\mathbf{r}}) e^{i\tilde{\phi}(\tilde{\mathbf{r}})}. \quad (20)$$

The BEC is located at the center of the numerical domain. The equilibrium state  $\tilde{\psi}_{\text{eq}}$  is obtained using the

imaginary time propagation method of the GPP equations. The initial phase is given by

$$\tilde{\phi}(\tilde{r}_\perp, \tilde{z}) = \frac{1}{2} \left( \tilde{\alpha} \tilde{r}_\perp^2 + \tilde{\beta} \tilde{z}^2 \right), \quad (21)$$

which yields the initial velocity field  $\tilde{\mathbf{v}} = \tilde{\nabla} \tilde{\phi} = (\tilde{\alpha} \tilde{r}_\perp) \mathbf{e}_\perp + (\tilde{\beta} \tilde{z}) \mathbf{e}_z$ . Here,  $\tilde{r}_\perp = \sqrt{\tilde{x}^2 + \tilde{y}^2}$  and  $\tilde{z}$  are the 3D cylindrical coordinates, and the unit vectors along each direction are  $\mathbf{e}_\perp$  and  $\mathbf{e}_z$ . We determine the initial velocity by  $\tilde{\alpha}$  and  $\tilde{\beta}$  (e.g., it becomes isotropic when  $\tilde{\alpha} = \tilde{\beta}$ ).

Finally, the physical and numerical parameters are denoted. We consider that each boson has a mass  $m = 3 \times 10^{-24}$  eV and an s-wave scattering length  $a = 5.62 \times 10^{-98} \lambda_c$  m, where  $\lambda_c$  is the Compton wavelength [46]. For the numerical analyses, we use a 3D cube of length  $\tilde{L}_x = \tilde{L}_y = \tilde{L}_z = 40$ . The scale factor is  $\tilde{\lambda} = 3 \times 10^{-3}$ , such that the numerical domain is much larger than the BEC. The spatial grid is set to  $\tilde{N}_x = \tilde{N}_y = \tilde{N}_z = 128$ . The time resolution of the GP equation is  $\Delta \tilde{t} = 10^{-3}$  and the resolution of the parameter  $\tilde{s}$  is  $0.05 \times (\tilde{L}_x / \tilde{N}_x)^2 \approx 4.88 \times 10^{-3}$ . The parameters of the sponge potential are  $\tilde{V}_o = 1000$ ,  $\tilde{r}_c = 0.8 \times (\tilde{L}_x / 2) = 16$  and  $\tilde{\delta} = 2 \times (\tilde{L}_x / \tilde{N}_x) = 0.625$ . Then,  $\tilde{r}_c$  is larger than the dimensionless TF radius  $\tilde{R}_{\text{TF}} \approx 9.09$ , which is the typical size of a BEC. This is reasonable because the sponge potential works outside the BEC. In all our simulations, the particles are hardly emitted from the BEC.

### III. BREATHING MODE

In this section, we consider the breathing modes of self-gravitating BEC. In the case of a typical BEC trapped by an external potential, the initial radial velocity field induces the breathing mode [14, 24, 54]. Similarly, we analytically and numerically study the breathing mode of a self-gravitating BEC by setting a spherically symmetric initial phase. Our numerical results are verified by comparing them with our analytical calculations.

#### A. ANALYTICAL CALCULATION BY VARIATIONAL METHOD

We apply the variational method to the GPP model to describe the breathing modes of self-gravitating BECs. We consider a self-gravitating BEC with a fixed total mass  $M$ . Previous studies used Gaussian [28] and quadratic functions [38] as the trial functions of the variational method. We adopt the 0-th spherical Bessel function as the trial function because we consider that the self-gravitating BEC have a large total mass, allowing us to use the TF approximation. This approach is the most appropriate for such a large total mass.

We prepare a trial function for applying the variational method. When the self-gravitating BEC is large that the

TF approximation is available, the macroscopic wavefunction of the equilibrium state is obtained as

$$\psi_{\text{eq}}(r) = \sqrt{\frac{\pi M}{4mR_{\text{TF}}^3}} j_0\left(\frac{\pi r}{R_{\text{TF}}}\right) \quad (22)$$

using Eqs. (8) and (11). Assuming that the density profile maintains its form as in Eq. (22) during the motion of the cloud, the trial function can obtain

$$\psi(\mathbf{r}, t) = \sqrt{\frac{\pi M}{4mR(t)^3}} j_0\left(\frac{\pi r}{R(t)}\right) \exp\left[i\frac{mr^2}{2\hbar}H(t)\right] \quad (23)$$

in the range of  $r < R(t)$  [14, 38, 39]. Then, we can consider the radius  $R(t)$  and  $H(t)$  as variables of breathing mode.

We obtain the Euler-Lagrange equations for  $R(t)$  and  $H(t)$ . The GPP model can be described by a Lagrangian

$$L = \frac{i\hbar}{2} \int d\mathbf{r} (\psi^* \partial_t \psi - \psi \partial_t \psi^*) - E, \quad (24)$$

using Eq. (4) [38]. Substituting the trial function (23), the Lagrangian becomes

$$L(R, H) = -\frac{1}{2} \left(1 - \frac{6}{\pi^2}\right) MR^2(\dot{H} + H^2) - U(R). \quad (25)$$

Here, the effective potential  $U(R)$  is

$$U(R) = \frac{\pi}{8} \frac{\hbar^2 M}{m^2 R^2} F(\Lambda) - \frac{3}{4} \frac{GM^2}{R} + \frac{\pi^2}{4} \frac{\hbar^2 a M^2}{m^3 R^3} \quad (26)$$

$$\equiv \frac{C_z}{R^2} - \frac{C_p}{R} + \frac{C_i}{R^3}.$$

Here the coefficients are  $C_z = \frac{\pi}{8} \frac{\hbar^2 M}{m^2} F(\Lambda)$ ,  $C_p = \frac{3}{4} GM^2$ , and  $C_i = \frac{\pi^2}{4} \frac{\hbar^2 a M^2}{m^3}$ , and the function  $F(\Lambda) = \text{Si}(\pi) - \pi + \int_0^{\Lambda\pi} dx \frac{x}{\sin x}$ . Hence, the Euler-Lagrange equation for  $H(t)$  is  $H(t) = \dot{R}(t)/R(t)$ , and the radius  $R(t)$  follows the equation:

$$\left(1 - \frac{6}{\pi^2}\right) M \frac{d^2 R(t)}{dt^2} = -\frac{dU(R)}{dR} \quad (27)$$

[61].

The equilibrium solution  $R_{\text{eq}}$  is obtained using  $dU(R)/dR = 0$  as

$$R_{\text{eq}} = \frac{C_z + \sqrt{C_z^2 + 3C_p C_i}}{C_p} \quad (28)$$

$$= \frac{\pi^2 \hbar^2}{6Gm^2} \frac{F(\Lambda)}{M} \left\{ 1 + \sqrt{1 + \frac{36Gam}{\pi^2 \hbar^2} \frac{M^2}{F(\Lambda)^2}} \right\}.$$

Fig. 1 describes the result of Eq. (28) when we set the cutoff parameter to  $\Lambda = 0.97$ . This figure shows that as the total mass  $M$  increases,  $R_{\text{eq}}$  decreases monotonically with gravity and converges to the TF radius of Eq. (9),

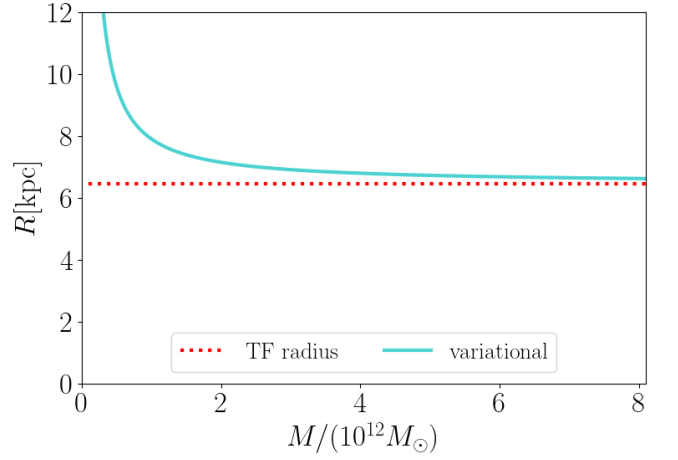


FIG. 1. The relation between the total mass  $M$  and the radius  $R$  derived by Eq. (9) when we set the cut-off parameter by  $\Lambda = 0.97$ . The horizontal axis shows the total mass, and the vertical axis shows the radius. The cyan solid line shows the analytical result of Eq. (9), and the red dotted line shows the TF radius  $R_{\text{TF}}$ .

for  $M \rightarrow \infty$ . Thus, our result can improve the relationship compared with previous studies [28, 38] using other trial functions when the total mass is large.

The breathing mode can be described as a small oscillation of radius around  $R_{\text{eq}}$ . The fluctuation is given by  $R(t) = R_{\text{eq}} + \delta R(t)$  ( $|\delta R(t)| \ll R_{\text{eq}}$ ). Using Eqs. (26), (27), and (28), we obtain the following equation of motion:

$$\frac{d^2 \delta R(t)}{dt^2} \simeq -\frac{\pi^2}{\pi^2 - 6} \frac{1}{M} \frac{d^2 U(R_{\text{eq}})}{dR^2} \delta R(t) \quad (29)$$

$$= -\frac{2\pi^2}{\pi^2 - 6} \frac{C_z R_{\text{eq}} + 3C_i}{M R_{\text{eq}}^5} \delta R(t).$$

Here, we consider the total mass of the BEC to be sufficiently large that the TF approximation is available. Because  $C_z$  is negligible, we can simplify Eq. (29) to

$$\frac{d^2 \delta R(t)}{dt^2} = -\frac{3}{2\pi(\pi^2 - 6)} \sqrt{\frac{G^5 m^9}{\hbar^6 a^3}} M \delta R(t), \quad (30)$$

which implies a harmonic oscillation with a period

$$T_B = 2\pi \sqrt{\frac{2\pi(\pi^2 - 6)}{3}} \sqrt{\frac{\hbar^6 a^3}{G^5 m^9}} \frac{1}{\sqrt{M}}. \quad (31)$$

The dependence on  $M$  was also reported in previous studies [28, 38]. The prefactor and  $M$ -dependence can be confirmed by the following numerical calculations.

## B. NUMERICAL RESULTS

In order to conform Eq. (31), we perform numerical simulations for the total mass  $M/(10^{14} M_\odot) = 1, 2, 3, 4$

with solar mass  $M_\odot$ . These values are much larger than typical values. For example, the Andromeda galaxy has  $M \sim 10^{12} M_\odot$  [36] and the Milky Way has  $M \simeq 0.5 - 2.0 \times 10^{12} M_\odot$  [55]. However, such a large total mass enables us to easily investigate the oscillation of the BEC because  $R_{\text{eq}}$  hardly change even if the total mass is reduced (see Fig 1). We set the parameters of the initial phase to  $\tilde{\alpha} = \tilde{\beta} = \pm 0.03, 0.1$  to add isotropic velocity to the equilibrium state.

First, we describe the time evolution of the density and gravitational potential profiles. In the simulations presented in this section, although the fully three-dimensional GPP equations are solved, the configurations of the BECs maintain spherical symmetry during the time evolution. Then, we consider the average of the density and gravitational potential over the solid angle to describe the time evolution such that

$$\rho(r, t) = \frac{1}{4\pi r^2 \Delta r} \int_{r-\frac{\Delta r}{2}}^{r+\frac{\Delta r}{2}} dr' r'^2 \int d\Omega \rho(\mathbf{r}', t) \quad (32)$$

and

$$V(r, t) = \frac{1}{4\pi r^2 \Delta r} \int_{r-\frac{\Delta r}{2}}^{r+\frac{\Delta r}{2}} dr' r'^2 \int d\Omega V(\mathbf{r}', t), \quad (33)$$

where  $\Omega$  denotes a solid angle and  $\Delta r \approx 0.22 \text{ kpc}$  is set as the dimensionless one is equal to the spatial resolution  $\Delta \tilde{r} = \tilde{L}_x / \tilde{N}_x = 0.3125$ . Fig. 2 shows the time evolution of the profiles of the density and gravitational potential. The BEC periodically undergo repeated spherical expansion and shrinkage. The BEC expands by adding the initial velocity directed outwards, and the central density decreases until  $t = 0.46 \text{ Myr}$ . Subsequently, the BEC shrinks, and the central density increases until  $t = 1.39 \text{ Myr}$ . Finally, the BEC returns to its initial state at  $t = 1.86 \text{ Myr}$ . The gravitational potential also oscillates simultaneously with the density profile. The gravitational potential becomes shallow when the central density decreases, and vice versa. Note that at the outskirts, namely, for  $r \gtrsim R_{\text{TF}} \approx 6.46 \text{ kpc}$ , the gravitational potential does not change during the time evolution, maintaining  $V = -GM/r$  because the total mass is constant.

To observe the spherical oscillation quantitatively, we define the effective radius  $R_{\text{eff}}$  as

$$R_{\text{eff}}(t) = \sqrt{\frac{1}{M} \int dr r^2 \rho(\mathbf{r}, t)}. \quad (34)$$

Using Eq. (23), it is proportional to the radius  $R(t)$ . Thus, when the self-gravitating BEC causes the breathing mode, the effective radius exhibits an oscillation similar to that of the radius. Figure 3(a) shows the change in effective radius from the initial value  $\Delta R_{\text{eff}}(t) = R_{\text{eff}}(t) - R_{\text{eff}}(0)$  to  $\tilde{\alpha} = 0.03$ . The graph shows sinusoidal curves for each total mass. The oscillation can be characterized by the period  $T_{R_{\text{eff}}}$  which decreases with

$M$ . Fig. 3(b) suggests that our results of  $T_{R_{\text{eff}}}$  agree quantitatively with Eq. (31), even for three values of  $\tilde{\alpha}$ . Therefore, we determine that the self-gravitating BEC causes the breathing mode.

## IV. APPEARANCE OF ANISOTROPIC MODE

### A. NUMERICAL RESULTS

We consider the axisymmetric collective mode of a self-gravitating BEC. Its total mass is  $M/(10^{14} M_\odot) = 1, 2, 3, 4$ , same as that in breathing mode. We can simulate these situations by setting  $(\tilde{\alpha}, \tilde{\beta}) = (\pm 0.03, 0), (0, \pm 0.03)$ . Such parameters introduce a non-spherical initial velocity to the equilibrium state of the BEC and can cause anisotropic oscillation.

In order to describe the time evolution of the BEC, we obtain the density and gravitational potential profiles by averaging  $\rho(\mathbf{r}, t)$  and  $V(\mathbf{r}, t)$ :

$$\rho(r_\perp, z, t) = \frac{1}{2\pi r_\perp \Delta r_\perp} \int_{r_\perp - \frac{\Delta r_\perp}{2}}^{r_\perp + \frac{\Delta r_\perp}{2}} dr'_\perp r'^2_\perp \int_0^{2\pi} d\theta \rho(r'_\perp, \theta, z, t) \quad (35)$$

and

$$V(r_\perp, z, t) = \frac{1}{2\pi r_\perp \Delta r_\perp} \int_{r_\perp - \frac{\Delta r_\perp}{2}}^{r_\perp + \frac{\Delta r_\perp}{2}} dr'_\perp r'^2_\perp \int_0^{2\pi} d\theta V(r'_\perp, \theta, z, t), \quad (36)$$

where  $\theta = \tan^{-1}(y/x)$  and  $\Delta r_\perp$  is set similar to  $\Delta r$ . Fig. 4 shows the density profile and the gravitational potential. They show simultaneous oscillations similar to those in the breathing mode. However,  $\rho(r_\perp, z = 0, t)$  is different from  $\rho(r_\perp = 0, z, t)$ . At  $t = 0.73 \text{ Myr}$ , the former shows an expansion of the BEC, but the latter shows shrinkage compared to the initial one. Subsequently, the density profile at  $t = 2.20 \text{ Myr}$  exhibits the opposite trend: a decrease in  $\rho(r_\perp, z = 0, t)$  and an increase in  $\rho(r_\perp = 0, z, t)$ . At  $t = 2.94 \text{ Myr}$ , the density profile returns to a spherical shape, similar to the initial profile. Hence, the self-gravitating BEC causes anisotropic oscillations due to the nonspherical initial velocity. We observe this behavior for other combinations of  $(\tilde{\alpha}, \tilde{\beta})$  such as  $\tilde{\alpha} \neq \tilde{\beta}$  (e.g.  $(\tilde{\alpha}, \tilde{\beta}) = (\pm 0.1, \mp 0.03)$ ).

To extract the effective degrees of freedom from the anisotropic oscillation, we introduce two quantities  $R_{\text{eff}}^\perp$  and  $Z_{\text{eff}}$ :

$$R_{\text{eff}}^\perp(t) = \sqrt{\frac{1}{M} \int dr r_\perp^2 \rho(\mathbf{r}, t)}, \quad (37)$$

$$Z_{\text{eff}}(t) = \sqrt{\frac{1}{M} \int dz z^2 \rho(\mathbf{r}, t)}. \quad (38)$$

These are the effective widths of the BEC in each direction;  $R_{\text{eff}}^\perp$  is the width in the direction of the radial

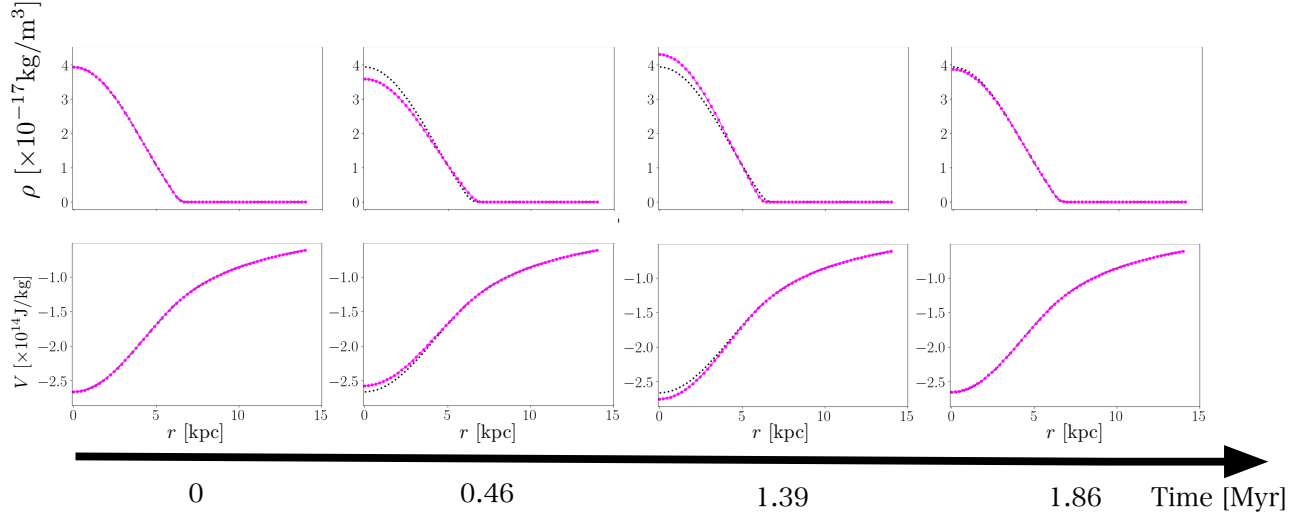


FIG. 2. The density profile and the gravitational potential of the self-gravitating BEC. The total mass is  $M = 2 \times 10^{14} M_{\odot}$  and the initial phase is set by  $\tilde{\alpha} = \tilde{\beta} = 0.1$ . The horizontal axis shows the radial coordinate, which is defined as the distance from the center of our numerical domain. Each column is the density profile or the gravitational potential at each time:  $t = 0, 0.46, 1.39, 1.86$  Myr, where Myr means a megayear. The magenta points show the data at each time, and the black dashed line shows the initial data. The upper row shows the density profile, and the vertical axis shows the density. The lower row shows the gravitational potential, and the vertical axis shows its value.

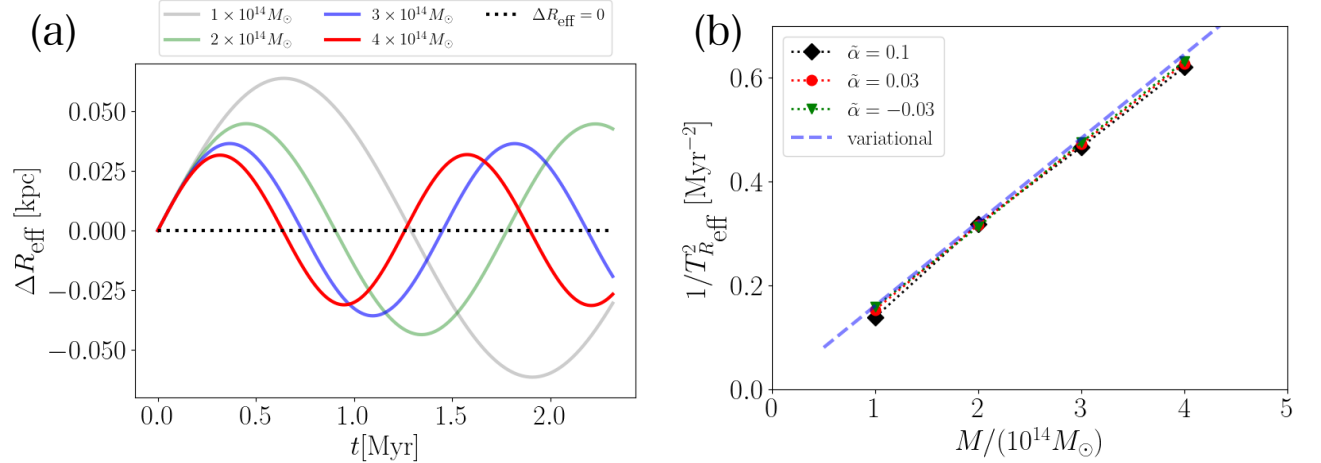


FIG. 3. Oscillation of the effective radius  $R_{\text{eff}}(t)$  for each total mass of the self-gravitating BEC. (a) The change of the effective radius from the initial/equilibrium one  $\Delta R_{\text{eff}}(t) = R_{\text{eff}}(t) - R_{\text{eff}}(0)$  when the initial phase is  $\tilde{\alpha} = 0.03$ . The horizontal axis shows the time, and the vertical axis shows  $\Delta R_{\text{eff}}(t)$ . Each solid curve is the time evolution of  $\Delta R_{\text{eff}}$  for each total mass (red:  $4 \times 10^{14} M_{\odot}$ , blue:  $3 \times 10^{14} M_{\odot}$ , green:  $2 \times 10^{14} M_{\odot}$  and black:  $1 \times 10^{14} M_{\odot}$ ). The black dotted line shows the oscillation criterion, namely  $\Delta R_{\text{eff}} = 0$ . (b) Total mass dependency on the period of the effective radius  $T_{R_{\text{eff}}}$  for each value of  $\tilde{\alpha}$ . The horizontal axis shows the total mass, and the vertical axis shows the minus squared period  $1/T_{R_{\text{eff}}}^2$ . Each point shows the numerical result (black square:  $\tilde{\alpha} = 0.1$ , red solid circle:  $\tilde{\alpha} = 0.03$  and green triangle:  $\tilde{\alpha} = -0.03$ ). The blue dashed line shows the analytical result of the variational method *i.e.* the minus squared period of breathing mode  $1/T_B^2$ .

coordinate  $r_{\perp}$  and  $Z_{\text{eff}}$  is the width in the direction of the  $z$ -axis. Fig. 5 shows the complicated oscillation of these quantities. The figure describes the opposite oscillation between  $R_{\text{eff}}^{\perp}$  and  $Z_{\text{eff}}$ . The BEC causes shrinkage in the direction of the  $z$ -axis when we initially provide a positive velocity in the direction of  $r_{\perp}$ , and vice versa. Similarly, the BEC shows shrinkage in the direction of  $r_{\perp}$  in response to the positive initial velocity in the direction

of the  $z$ -axis, and vice versa.

Although  $R_{\text{eff}}^{\perp}$  and  $Z_{\text{eff}}$  exhibit complex oscillations, a harmonic oscillation can be obtained from the ratio  $Z_{\text{eff}}/R_{\text{eff}}^{\perp}$ , as shown in Fig. 6. Among the four cases, the oscillations has a common amplitude and frequency despite the different behaviors of  $R_{\text{eff}}^{\perp}$ ,  $Z_{\text{eff}}$ . The ratio  $Z_{\text{eff}}/R_{\text{eff}}^{\perp}$  indicates the extent to which the BEC is axially deformed from a spherical shape, similar

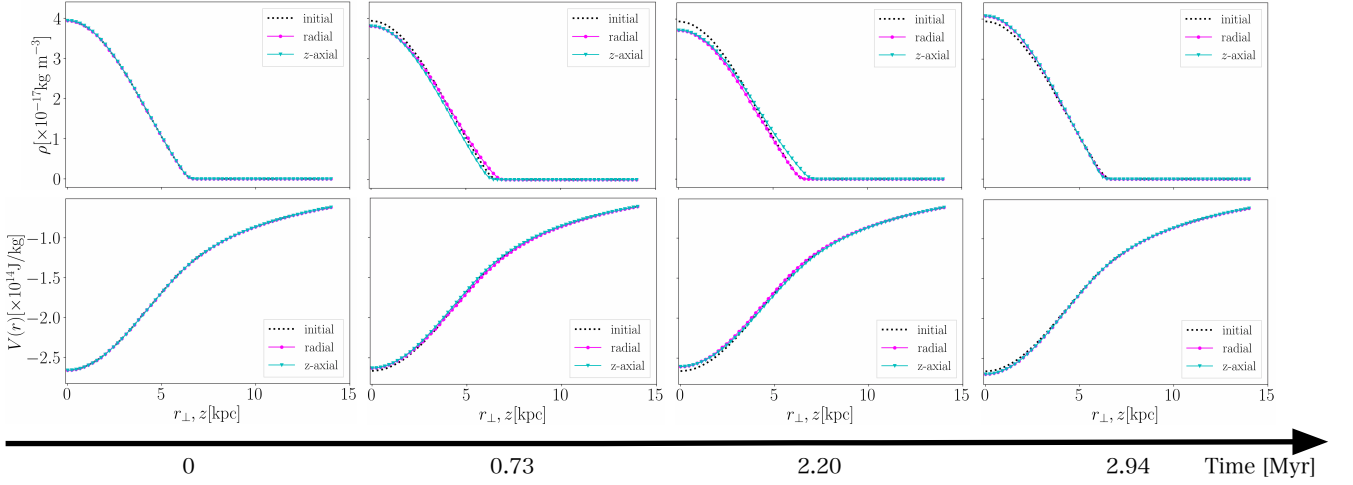


FIG. 4. The time evolution of the density profile  $\rho(r_{\perp}, z)$  and the gravitational potential  $V(r_{\perp}, z)$ . We consider the BEC has the total mass  $M = 2 \times 10^{14} M_{\odot}$  and is added the initial velocity by  $\tilde{\alpha} = 0.1, \tilde{\beta} = 0$ . The horizontal axis shows  $r_{\perp}$  and  $z$ . The magenta points show the profiles when  $z = 0$ , namely  $\rho(r_{\perp}, z = 0)$  and  $V(r_{\perp}, z = 0)$ , and the cyan triangles show the ones when  $r_{\perp} = 0$ , namely  $\rho(r_{\perp} = 0, z)$  and  $V(r_{\perp} = 0, z)$ . The black dashed lines show the initial profile. Each column shows the density profile or the gravitational potential at each time:  $t = 0, 0.73, 2.20, 2.94$  Myr, where Myr means a megayear. The upper row shows the density profile, and the vertical axis shows the density. The lower row shows the gravitational potential, and the vertical axis shows its value.

to the aspect ratio of the BEC. We can predict that one of the coupled modes is the quadrupole mode because the harmonic mode of the aspect ratio suggests a quadrupole mode of the BEC [56–58].

The Fourier transformation is useful for decomposing complicated oscillations into eigenmodes. Fig. 7 shows the Fourier transformation of  $R_{\text{eff}}^{\perp}$  and  $Z_{\text{eff}}/R_{\text{eff}}^{\perp}$  shown in Fig. 5 and Fig. 6. We can find two peaks of  $R_{\text{eff}}^{\perp}$  and a peak of  $Z_{\text{eff}}/R_{\text{eff}}^{\perp}$ . The high-frequency peak of  $R_{\text{eff}}^{\perp}$  corresponds to the breathing mode  $T_B$  of the BEC with the same total mass. On the other hand, the low-frequency peak of  $R_{\text{eff}}^{\perp}$  is similar to that of  $Z_{\text{eff}}/R_{\text{eff}}^{\perp}$ . This peak suggests the frequency of the quadrupole mode of the BEC. Therefore, the self-gravitating BEC causes an anisotropic collective mode in which the quadrupole mode superposes the breathing mode by the axisymmetric initial velocity.

Finally, we change the parameters of the initial phase and total mass to investigate the dependence of the period of  $Z_{\text{eff}}/R_{\text{eff}}^{\perp}$  on these quantities. Although we study the dynamics of some combinations of  $\tilde{\alpha}$  and  $\tilde{\beta}$ , the period is constant for all the simulations. Hence, the period  $Z_{\text{eff}}/R_{\text{eff}}^{\perp}$  is independent of the initial velocity. However, the total mass can change the period of  $Z_{\text{eff}}/R_{\text{eff}}^{\perp}$ , as shown in Fig. 8. Fig. 8 (a) shows that  $Z_{\text{eff}}/R_{\text{eff}}^{\perp}$  exhibits the harmonic oscillation similar to  $R_{\text{eff}}^{\perp}$  of the breathing mode by the isotropic initial velocity; the period become short as the total mass increases. The  $M$ -dependence of the period of  $Z_{\text{eff}}/R_{\text{eff}}^{\perp}$  and a comparison with  $T_B$  are shown in Fig. 8 (b). We find that  $Z_{\text{eff}}/R_{\text{eff}}^{\perp}$  clearly shows a straight line parallel to  $T_B$  in the log-log plot, suggesting that the period of the quadrupole mode is also inversely proportional to  $\sqrt{M}$ , similar to

the breathing mode. However, the period of  $Z_{\text{eff}}/R_{\text{eff}}^{\perp}$  is approximately 1.57 times larger than  $T_B$ ; the quadrupole mode is, in other words, the lower frequency oscillation than the breathing mode. This property can be observed in atomic BECs trapped by an isotropic harmonic potential. The frequency of the breathing mode is  $\sqrt{5/2}$  times as large as that of the quadrupole mode [24]. Hence, our numerical results are consistent with those of typical atomic BECs trapped by external potentials. The ratio of the period of  $Z_{\text{eff}}/R_{\text{eff}}^{\perp}$  to  $T_B$  is close to that of the BEC trapped by an isotropic harmonic potential. Moreover, the periods of  $Z_{\text{eff}}/R_{\text{eff}}^{\perp}$  are in good agreement with  $\sqrt{5/2}T_B$  (see Fig. 8). Thus, the numerical results indicate that the quadrupole mode has the period  $\sqrt{5/2}T_B$ . In order to reproduce our numerical results, we extend the variational method of the spherical self-gravitating BEC in Sec.III-A to the axisymmetric system in the following subsection.

## B. ANALYSIS OF AXISYMMETRIC COLLECTIVE MODE BY VARIATIONAL METHOD

Rindler-Daller and Shapiro extended the TF solution to an ellipsoidal self-gravitating BEC [16, 37] using the ellipsoidal approximation [59]. Considering that the self-gravitating BEC takes a spheroidal configuration with semi-axes  $R_{\perp}$  and  $Z$ , the extended TF solution is written as

$$\rho(q) = \frac{\pi M}{4R_{\perp}^2 Z} j_0 \left( \frac{\pi q}{R_{\perp}} \right), \quad (39)$$

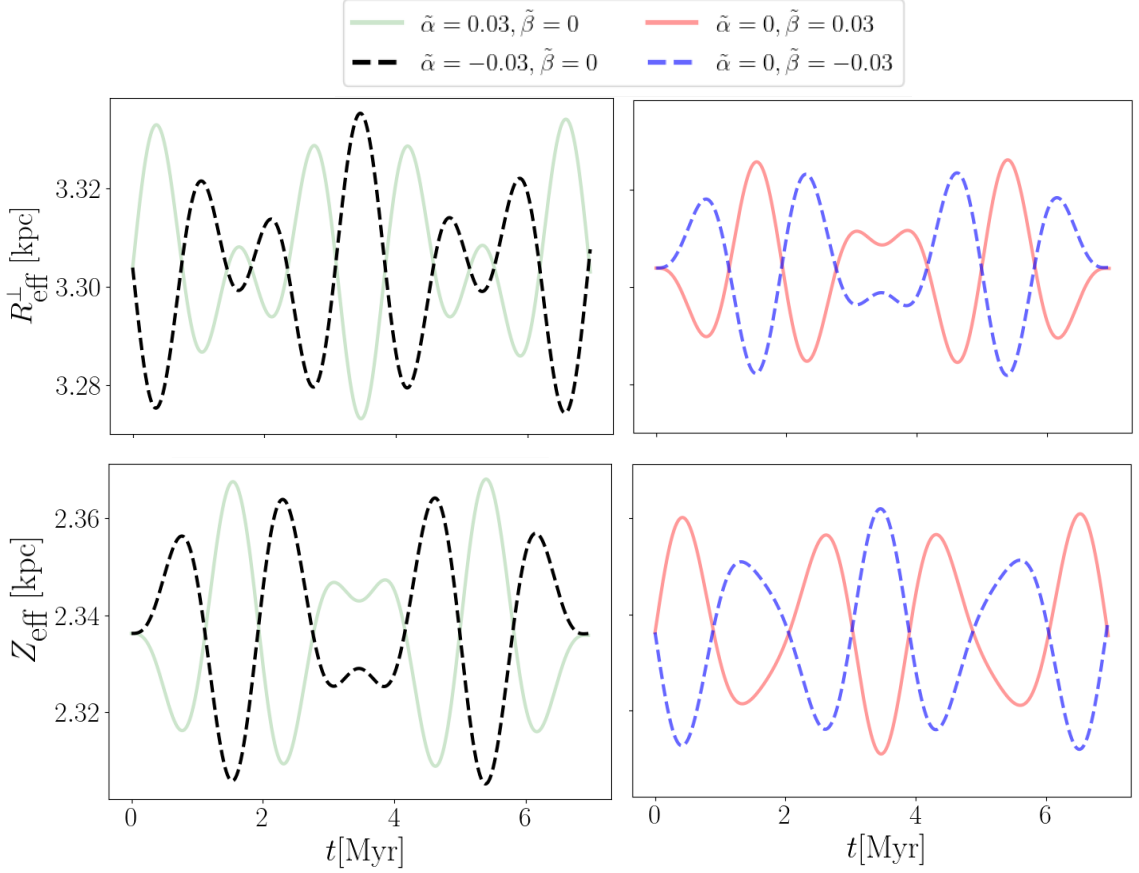


FIG. 5. Oscillations of the effective width  $R_{\text{eff}}^{\perp}$ ,  $Z_{\text{eff}}$ . The self-gravitating BEC has the total mass  $M = 4 \times 10^{14} M_{\odot}$  and the initial velocity is set by  $(\tilde{\alpha}, \tilde{\beta}) = (\pm 0.03, 0)$ ,  $(0, \pm 0.03)$ . The vertical axis shows the time. The left column shows the result of  $(\tilde{\alpha}, \tilde{\beta}) = (\pm 0.03, 0)$ , which means the initial velocity in the direction of  $r_{\perp}$ . The green solid line shows the oscillation when the BEC initially expands ( $\tilde{\alpha} > 0$ ), and the black broken line shows the oscillation when the BEC initially shrinks ( $\tilde{\alpha} < 0$ ). On the other hand, the right column shows the result of  $(\tilde{\alpha}, \tilde{\beta}) = (0, \pm 0.03)$ , which means the initial velocity in the direction of the  $z$ -axis. The red solid line shows the oscillation when the BEC initially expands ( $\tilde{\beta} > 0$ ), and the blue broken line shows the oscillation when the BEC initially shrinks ( $\tilde{\beta} < 0$ ). While the upper row shows the time evolution of  $R_{\text{eff}}^{\perp}$ , the lower row shows the time evolution of  $Z_{\text{eff}}$ .

where  $M$  is the total mass and  $q \in (0, R_{\perp}]$  satisfies  $(q/R_{\perp})^2 = (r_{\perp}/R_{\perp})^2 + (z/Z)^2$ . To obtain the density profiles in Eq. (39), the trial function is set as

$$\psi(\mathbf{r}, t) = \sqrt{\frac{\pi M}{4mR_{\perp}(t)^2 Z(t)}} j_0\left(\frac{\pi q}{R_{\perp}(t)}\right) \times \exp\left[i\frac{m}{2\hbar}(r_{\perp}^2 H_{\perp}(t) + z^2 H_z(t))\right], \quad (40)$$

where  $H_{\perp}(t)$  and  $H_z(t)$  are variables that provide the velocity field such that

$$\mathbf{v} = (r_{\perp} H_{\perp}(t)) \mathbf{e}_{\perp} + (z H_z(t)) \mathbf{e}_z. \quad (41)$$

The Lagrangian can be obtained by substituting Eq. (40) to its definition (24). Using Eq. (40), the energy components  $K$ ,  $W$ ,  $I$  defined by Eqs. (5), (6), and (7)

are

$$K \simeq \frac{\pi}{24} \frac{\hbar^2 M}{m^2} F(\Lambda) \left( \frac{2}{R_{\perp}(t)^2} + \frac{1}{Z(t)^2} \right) + \frac{M}{6} \frac{\pi^2 - 6}{\pi^2} \{2H_{\perp}(t)^2 R_{\perp}(t)^2 + H_z(t)^2 Z(t)^2\} \quad (42)$$

$$W = -\frac{3GM^2}{4} \frac{1}{\{R_{\perp}(t)^2 Z(t)\}^{1/3}}, \quad (43)$$

$$I = \frac{\pi^2}{4} \frac{\hbar^2 a M^2}{m^3} \frac{1}{R_{\perp}(t)^2 Z(t)}, \quad (44)$$

where Eq. (43) can be derived using the formula for the gravitational energy of the spheroidal density profile in [4]. We assume that the deformation of the BEC is sufficiently small [62]. Hence, the Lagrangian can be written

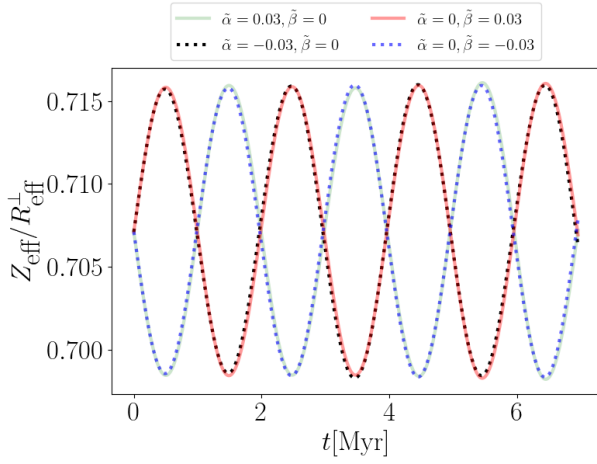


FIG. 6. The oscillation of the ratio  $Z_{\text{eff}}/R_{\text{eff}}^{\perp}$  when the total mass of the self-gravitating BEC is  $M = 4 \times 10^{14} M_{\odot}$ . The horizontal axis shows the time, and the vertical axis shows the value of the ratio  $Z_{\text{eff}}/R_{\text{eff}}^{\perp}$ . The solid lines show the initially expanding cases (green: the direction of  $r_{\perp}$  and red: the direction of the  $z$ -axis), and the dotted lines show the initially shrinking cases (black: the direction of  $r_{\perp}$  and blue: the direction of the  $z$ -axis).

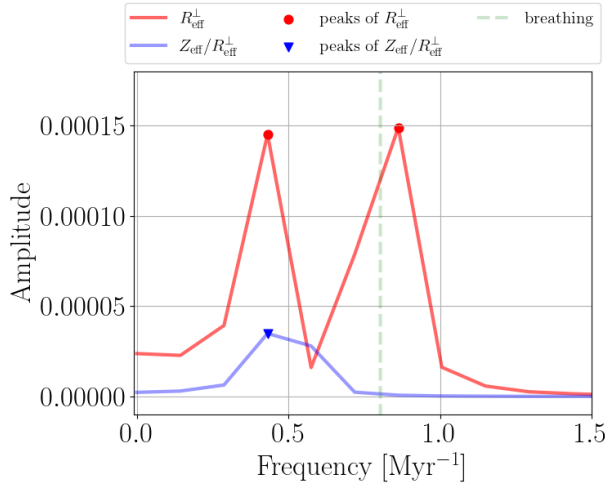


FIG. 7. The Fourier transform of  $R_{\text{eff}}^{\perp}$  and  $Z_{\text{eff}}/R_{\text{eff}}^{\perp}$ . The self-gravitating BEC has the total mass  $M = 4 \times 10^{14} M_{\odot}$  and the initial velocity given by  $\tilde{\alpha} = 0.03$ ,  $\tilde{\beta} = 0$ . The horizontal axis shows the frequency, and the vertical axis shows the amplitude. The solid lines show the results of each transformation (red:  $R_{\text{eff}}^{\perp}$  and blue:  $Z_{\text{eff}}/R_{\text{eff}}^{\perp}$ ), and the green broken line shows the analytical/variational result of the breathing mode  $T_B$ . The red points show the peaks of  $R_{\text{eff}}^{\perp}$ , and the blue triangle shows the peak of  $Z_{\text{eff}}/R_{\text{eff}}^{\perp}$ .

as

$$L(R_{\perp}, Z, H_{\perp}, H_z) = -\frac{\pi^2 - 6}{6\pi^2} M \left\{ 2R_{\perp}^2 (\dot{H}_{\perp} + H_{\perp}^2) + Z^2 (\dot{H}_z + H_z^2) \right\} - U(R_{\perp}, Z). \quad (45)$$

Here, the effective potential  $U(R_{\perp}, Z)$  is defined as

$$U(R_{\perp}, Z) = \frac{C_z}{3} \left( \frac{2}{R_{\perp}^2} + \frac{1}{Z^2} \right) - \frac{C_p}{(R_{\perp}^2 Z)^{1/3}} + \frac{C_i}{R_{\perp}^2 Z}, \quad (46)$$

where  $C_z$ ,  $C_p$  and  $C_i$  are identical to those in Eq. (26). The Euler-Lagrange equations for  $H_{\perp}(t)$  and  $H_z(t)$  are  $H_{\perp}(t) = \dot{R}_{\perp}(t)/R_{\perp}(t)$  and  $H_z(t) = \dot{Z}(t)/Z(t)$ . Therefore, the Euler-Lagrange equations for  $R_{\perp}(t)$  and  $Z(t)$  are

$$\begin{cases} \frac{2}{3} \frac{\pi^2 - 6}{\pi^2} M \frac{d^2 R_{\perp}(t)}{dt^2} = -\frac{\partial U(R_{\perp}, Z)}{\partial R_{\perp}}, \\ \frac{1}{3} \frac{\pi^2 - 6}{\pi^2} M \frac{d^2 Z(t)}{dt^2} = -\frac{\partial U(R_{\perp}, Z)}{\partial Z}. \end{cases} \quad (47)$$

These Euler-Lagrange equations show the spherical equilibrium state with  $R_{\perp} = Z = R_{\text{eq}}$ , which is consistent with the results in Sec.III-A.

Similar to the spherically symmetric case, we consider a small oscillation of the semi-axes near  $R_{\text{eq}}$ . The fluctuations in the semi-axes are given by  $R_{\perp}(t) = R_{\text{eq}} + \delta R_{\perp}(t)$  and  $Z(t) = R_{\text{eq}} + \delta Z(t)$  ( $|\delta R_{\perp}(t)|, |\delta Z(t)| \ll R_{\text{eq}}$ ). The equations of motion for the fluctuations  $\delta R_{\perp}(t)$  and  $\delta Z(t)$  are

$$\begin{aligned} & \frac{3(\pi^2 - 6)}{\pi^2} M R_{\text{eq}}^5 \frac{d^2}{dt^2} \begin{pmatrix} 2\delta R_{\perp}(t) \\ \delta Z(t) \end{pmatrix} \\ &= - \begin{pmatrix} 4C_p R_{\text{eq}}^2 & 2(-C_p R_{\text{eq}}^2 + 9C_i) \\ -C_p R_{\text{eq}}^2 + 9C_i & 5C_p R_{\text{eq}}^2 - 9C_i \end{pmatrix} \begin{pmatrix} 2\delta R_{\perp}(t) \\ \delta Z(t) \end{pmatrix}. \end{aligned} \quad (49)$$

If we write the solutions as  $2\delta R_{\perp}(t) = A \exp[i\omega t]$  and  $\delta Z(t) = B \exp[i\omega t]$ , then the angular frequency  $\omega$  satisfies

$$\omega = \pm \sqrt{\frac{2\pi^2}{\pi^2 - 6} \frac{C_z R_{\text{eq}} + 3C_i}{M R_{\text{eq}}^5}} \equiv \pm \omega_B, \quad (50)$$

or

$$\omega = \pm 2 \sqrt{\frac{\pi^2}{\pi^2 - 6} \frac{C_z}{M R_{\text{eq}}^4}} \equiv \pm \omega_Q. \quad (51)$$

Eq. (50) provides the eigenfrequency of the breathing mode compared to the coefficient of Eq. (29). Indeed, when  $\omega = \pm \omega_B$ , the eigenmodes satisfy  $A = 2B$  *i.e.*

$$\begin{pmatrix} \delta R_{\perp}(t) \\ \delta Z(t) \end{pmatrix} = A \begin{pmatrix} 1 \\ 1 \end{pmatrix} \exp[\pm i\omega_B t]. \quad (52)$$

This indicates that the BEC either expands spherically or shrinks. On the other hand, when  $\omega = \pm \omega_Q$ , the eigenmodes satisfy  $A + B = 0$  *i.e.*

$$\begin{pmatrix} \delta R_{\perp}(t) \\ \delta Z(t) \end{pmatrix} = A \begin{pmatrix} 1 \\ -2 \end{pmatrix} \exp[\pm i\omega_Q t]. \quad (53)$$

We can consider Eq. (53) as the quadrupole mode because it shows that the BEC is stretched along the  $z$ -axis or expanded along the  $xy$ -plane.

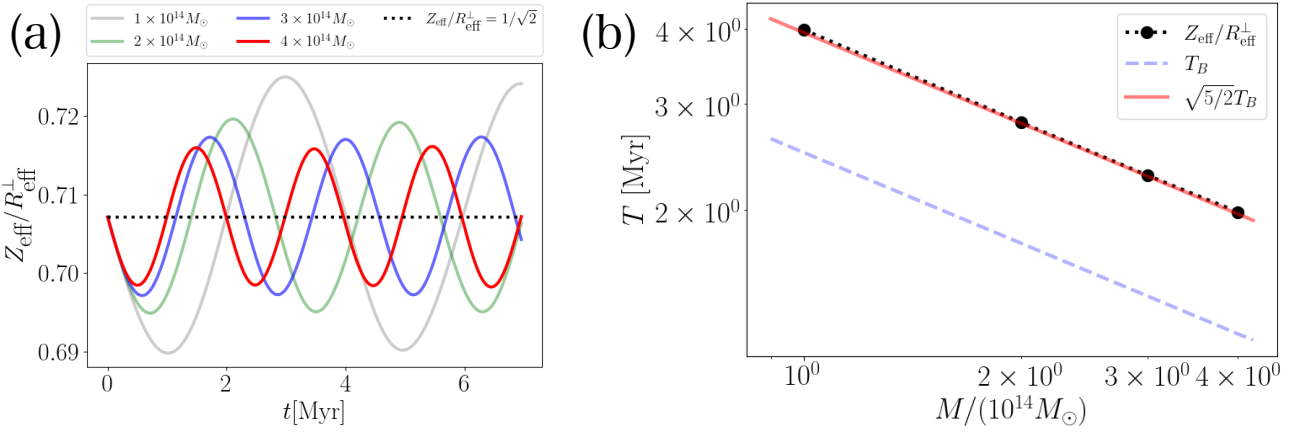


FIG. 8. The oscillation of  $Z_{\text{eff}}/R_{\text{eff}}^{\perp}$  for each total mass. The initial phase is set by  $\tilde{\alpha} = 0.03, \tilde{\beta} = 0$ . (a) The time evolution of  $Z_{\text{eff}}/R_{\text{eff}}^{\perp}$  for each total mass. The horizontal axis shows the time, and the vertical axis shows the value of  $Z_{\text{eff}}/R_{\text{eff}}^{\perp}$ . The black dotted line shows the ratio when the BEC is in the equilibrium state; the ratio becomes  $Z_{\text{eff}}/R_{\text{eff}}^{\perp} = 1/\sqrt{2}$ . Each solid line shows the result (red:  $4 \times 10^{14} M_{\odot}$ , blue:  $3 \times 10^{14} M_{\odot}$ , green:  $2 \times 10^{14} M_{\odot}$ , black:  $1 \times 10^{14} M_{\odot}$ ). (b) The total mass dependence of the period of  $Z_{\text{eff}}/R_{\text{eff}}^{\perp}$  by the log-log plot. The horizontal axis shows the total mass, and the vertical axis shows the period. The black points show the numerical results for each total mass, while the blue broken line shows the variational result of the breathing mode  $T_B$ . The red solid line shows  $\sqrt{5/2} T_B$ .

We compare Eqs. (52) and (53) with the numerical results. In our numerical simulations, we set two initial conditions:  $\delta R_{\perp}(t=0) = \delta Z(t=0) = 0$  and  $\tilde{\mathbf{v}}(\tilde{t} =$

$0, \tilde{r}_{\perp}, \tilde{z}) = \tilde{\alpha} \tilde{r}_{\perp} \mathbf{e}_{\perp} + \tilde{\beta} \tilde{z} \mathbf{e}_z$ . As a result, the fluctuations  $\delta R_{\perp}(t)$  and  $\delta Z(t)$  become

$$\delta R_{\perp}(t) = \frac{\tilde{\lambda}^2 c^2 m R_{\text{eff}}}{3\hbar} \left\{ \frac{2\tilde{\alpha} + \tilde{\beta}}{\omega_B} \sin(\omega_B t) + \frac{\tilde{\alpha} - \tilde{\beta}}{\omega_Q} \sin(\omega_Q t) \right\}, \quad (54)$$

and

$$\delta Z(t) = \frac{\tilde{\lambda}^2 c^2 m R_{\text{eff}}}{3\hbar} \left\{ \frac{2\tilde{\alpha} + \tilde{\beta}}{\omega_B} \sin(\omega_B t) - 2 \frac{\tilde{\alpha} - \tilde{\beta}}{\omega_Q} \sin(\omega_Q t) \right\}. \quad (55)$$

The effective widths  $R_{\text{eff}}^{\perp}$  and  $Z_{\text{eff}}$  respectively result in  $R_{\text{eff}}^{\perp} = \sqrt{2/3} \sqrt{(\pi^2 - 6)/\pi^2} R_{\perp}$  and  $Z_{\text{eff}} = \sqrt{(\pi^2 - 6)/(3\pi^2)} Z$  using Eq. (40). Thus we can find

$$\frac{Z_{\text{eff}}}{R_{\text{eff}}^{\perp}} = \frac{Z}{\sqrt{2} R_{\perp}} \simeq \frac{1}{\sqrt{2}} - \frac{\tilde{\lambda}^2 c^2 m (\tilde{\alpha} - \tilde{\beta})}{\sqrt{2} \hbar \omega_Q} \sin(\omega_Q t), \quad (56)$$

which show that the quadrupole mode causes a harmonic oscillation of  $Z_{\text{eff}}/R_{\text{eff}}^{\perp}$  at near  $1/\sqrt{2}$ . This confirms that the quadrupole mode appears in the numerical simulations (Fig. 6 or Fig. 8 (a) in Sec. IV-A).

Our variational calculation of the axisymmetric self-gravitating BEC suggests that we can obtain only the quadrupole mode by selecting an appropriate initial phase. As the first term on the right-hand side of Eqs. (54) and (55) disappear, we can extract only the quadrupole mode by setting the initial phase as  $2\tilde{\alpha} + \tilde{\beta} =$

0. Then, the quadrupole mode shows

$$\delta R_{\perp}(t) = \frac{\tilde{\alpha} \tilde{\lambda}^2 c^2 m R_{\text{eq}}}{\hbar \omega_Q} \sin(\omega_Q t) \quad (57)$$

and

$$\delta Z(t) = -2 \frac{\tilde{\alpha} \tilde{\lambda}^2 c^2 m R_{\text{eq}}}{\hbar \omega_Q} \sin(\omega_Q t), \quad (58)$$

which leads to harmonic oscillations of  $R_{\text{eff}}^{\perp}$  and  $Z_{\text{eff}}$  in the opposed phase. Indeed, we can numerically extract only the quadrupole mode when the total mass is  $M = 4 \times 10^{14} M_{\odot}$  and the initial phase is set as  $\tilde{\alpha} = 0.03$  and  $\tilde{\beta} = -0.06$ , as shown in Fig. 9. This figure shows that  $\Delta R_{\text{eff}}^{\perp} \equiv R_{\text{eff}}^{\perp}(t) - R_{\text{eff}}^{\perp}(0)$  and  $\Delta Z_{\text{eff}} \equiv Z_{\text{eff}}(t) - Z_{\text{eff}}(0)$  oscillate monotonically in the opposed-phase and their periods are the same as that shown in Fig. 6. Additionally, the amplitude of  $\Delta Z_{\text{eff}}$  is approximately 1.40 times

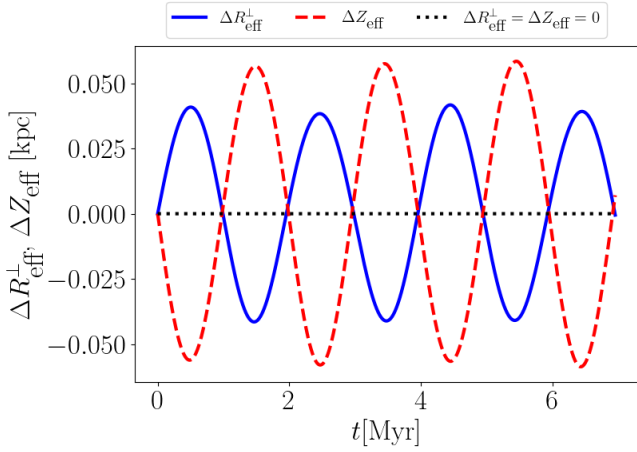


FIG. 9. The oscillation of the change of the effective widths  $\Delta R_{\text{eff}}^{\perp} = R_{\text{eff}}^{\perp}(t) - R_{\text{eff}}^{\perp}(0)$  and  $\Delta Z_{\text{eff}} = Z_{\text{eff}}(t) - Z_{\text{eff}}(0)$  when the total mass is  $M = 4 \times 10^{14} M_{\odot}$  and the initial phase is set by  $\tilde{\alpha} = 0.03$  and  $\tilde{\beta} = -0.06$ . The horizontal axis shows the time, and the vertical axis shows  $\Delta R_{\text{eff}}^{\perp}$  and  $\Delta Z_{\text{eff}}$ . The blue solid line shows the time evolution of  $\Delta R_{\text{eff}}^{\perp}$ , and the red broken line shows the time evolution of  $\Delta Z_{\text{eff}}$ . The black dotted line shows that  $\Delta R_{\text{eff}}^{\perp} = \Delta Z_{\text{eff}} = 0$ .

greater than that of  $\Delta R_{\text{eff}}^{\perp}$ , which is consistent with our analysis because Eqs. (57) and (58) predict that the ratio of the amplitudes of  $\Delta Z_{\text{eff}}$  and  $\Delta R_{\text{eff}}^{\perp}$  is  $\sqrt{2}$ . Therefore, we successfully extract only the quadrupole mode of self-gravitating BEC.

Although this variational method agrees qualitatively with the numerical results, the frequency or period of the quadrupole mode does not agree with them. The ratio of  $\omega_Q$  to  $\omega_B$  is

$$\frac{\omega_Q}{\omega_B} = 2\sqrt{\frac{C_z R_{\text{eq}}}{C_p R_{\text{eq}}^2 + 3C_i}} \quad (59)$$

by Eqs. (28), (50) and (51). However, this ratio almost vanishes because we use  $C_p R_{\text{eq}}^2 \simeq 3C_i$  and  $C_z R_{\text{eq}} \ll C_i$  in the TF approximation. This is clearly different from the numerical results that show that  $\omega_Q/\omega_B = \sqrt{2/5}$  (see Fig. 8 (b)). This discrepancy is because the trial function in Eq. (40) is based on the TF solution. This approximation neglects the kinetic energy contribution and is broken near the surface of the BEC. However, Eqs. (13) and (51) show that the kinetic energy of the equilibrium state primarily determine the frequency of the quadrupole mode. Indeed, the quadrupole mode does not oscillate the central density, and neither the potential energy nor the self-interaction energy contributes to it. Consequently, the quadrupole mode can only change the BEC near the surface where the TF solution is broken down. Hence, a trial function based on the TF approximation does not allow us to quantitatively evaluate the contribution of the kinetic energy of the equilibrium state. This affects the frequency of the quadrupole mode. We must implement a first-order correction to

the kinetic energy of the equilibrium state of the self-gravitating BEC to quantitatively compare  $\omega_Q$  with the numerical results. This investigation will be conducted in a future study.

## V. CONCLUSIONS

We study the collective modes of the self-gravitating BECs. In particular, we focus on breathing and anisotropic collective modes. In this study, we show the following three aspects.

A self-gravitating BEC can induce a breathing mode by adding an isotropic initial velocity to its equilibrium state. Because of the density dependence of self-gravity, the gravitational potential near the center of the BEC oscillates with the density profile. The breathing mode of an ordinary BEC trapped by an external potential is characterized by the harmonic oscillation of the radius of the BEC, as similar to a self-gravitating BEC. However, as the total mass increases, the self-gravitating BEC reduces its amplitude and shortens its period. Moreover, the self-gravitating BEC indicates that the period of the breathing mode is inversely proportional to  $\sqrt{M}$ , which differs from an ordinal BEC trapped by a harmonic potential. This unique property clearly reflects the density dependence of self-gravity.

The axisymmetric initial velocity results in an anisotropic collective mode. It is found that the quadrupole mode is mixed with the breathing mode in the oscillation because the aspect ratio shows the harmonic oscillation for any choice of the initial velocity. The quadrupole mode also depends on the total mass. The amplitude and period decreases as the total mass increases, similar to the radius of the breathing mode. In addition, the period of the quadrupole mode has the same  $M$ -dependence as that of the breathing mode. Thus, it is inversely proportional to  $\sqrt{M}$ . This property is different from that of ordinary BECs trapped by an external potential. On the other hand, the ratio of the period of the quadrupole mode to that of the breathing mode is  $\sqrt{5/2}$ , as indicates by the BEC trapped by the isotropic harmonic potential.

We can extract only the quadrupole mode from the anisotropic collective mode by selecting an appropriate initial velocity. We extend the variational method, in which the trial function is based on the TF solution, to a spheroidal configuration. This result describes the anisotropic collective mode of the self-gravitating BEC and suggests the appropriate initial condition under which only the quadrupole mode occurs. We can numerically obtain the predicted results using the variational method. However, this variational method does not allow the evaluation of the kinetic energy of the equilibrium state. Consequently, it can not provide the proper frequency of the quadrupole mode because the frequency is determined by the contribution of the kinetic energy to the equilibrium state of the self-gravitating BEC. In

order to quantitatively reproduce the frequency, we may have to implement a first-order correction of the kinetic energy.

When the oscillation has a large amplitude, the density dependence of the self-gravitating BEC probably changes the  $M$ -dependence of the periods and other characteristics of the collective mode. In this study, we consider the amplitude to be small. However, the large deformation of a self-gravitating BEC affects the gravitational energy. Considering the deformation, a collective mode with a large amplitude can cause some nontrivial phenomena (e.g., the emergence of differences in whether the spheroidal configuration is oblate or prolate).

Collective modes may occur when several BECs collide and merge. The oscillations are characterized by eigenfrequency, which enable us to analyze the oscillation of the BEC after these phenomena. The existence of self-interaction is important because it determines the frequency, at least in the TF regime. In other words, we can observe the self-interaction effects of the self-gravitating BEC by the collective mode after the collision and merger.

We expect the collective modes of a self-gravitating BEC to be touchstones for the possibility that a dark matter halo is a BEC under self-gravity. In early studies on atomic BEC, its collective modes played a role in judging whether the system is a BEC. If Bose-Einstein condensation occurs and the BEC is formed in the universe, it is natural that the self-gravitating BEC exhibits such collective modes. In particular, anisotropic collective modes can emit the gravitational wave. Because the frequency of the collective mode of the self-gravitating BEC

reflects the mass of the Bose particle and self-interaction, we can estimate these quantities from observations of the gravitational wave. Thus, this approach suggests a new method for identifying dark matter.

One of our interests is the collective mode of the rotating self-gravitating BEC. In the universe, an object is generally not at rest but rotates or oscillates, and dark matter halos are no exception. The equilibrium state of a self-gravitating BEC is affected by rotation owing to its density dependence. For example, the quantized vortex in a BEC locally pushes the density through rotation, changing the density profile of the equilibrium state. Its gravitational potential is also different from that of a BEC without a quantized vortex. Hence, the self-gravitating BEC with a rotation or quantized vortex probably provides quite different phenomena of the collective modes from those in the present work.

## ACKNOWLEDGMENTS

We thank M. Kobayashi and Y. Sano for their fruitful discussions of our numerical calculations. This work was supported by JST and the establishment of university fellowships for the creation of science and technology innovation, Grant Number JPMJFS2138. M. T. acknowledges the support from JSPS KAKENHI Grant Number JP23K03305. This study was partially supported by Osaka Central Advanced Mathematical Institute. MEXT Joint Usage/Research Center on Mathematics and Theoretical Physics, JPMXP0619217849.

- 
- [1] V. Rubin and W. Ford, *Astrophys. J.*, **159**, 379 (1970).
  - [2] A. Refregier, *Annu. Rev. Astron. Astrophys.* **41**, 645 (2003).
  - [3] K. Freese, *EAS*, **36**, 113 (2009).
  - [4] J. Binney and S. Tremaine, *GALACTIC DYNAMICS*, second edition, (Princeton University Press, 2008).
  - [5] A. D. Popolo and M. L. Delliou, *galaxies*, **5**, 1, 17 (2017).
  - [6] A. Banerjee, K. K. Boddy, F. -Y. Cyr-Racine, A. L. Erickcek, D. Gilman, B. V. Lehmann, Y. -Y. Mao, P. Mocz, F. Munshi, E. O. Nadler, L. Necib, A. Parikh, A. H. G. Peter, L. Sales, M. Vogelsberger and A. C. Wright, *arXiv:2203.07049* (2022).
  - [7] W. Hu, R. Barkana and A. Gruzinov, *Phys. Rev. Lett.* **85**, 1158 (2000).
  - [8] L. Hui, *Annu. Rev. Astron. Astrophys.*, **59**, 247 (2021).
  - [9] D. N. Spergel and P. J. Steinhardt, *Phys. Rev. Lett.*, **84**, 3760 (2000).
  - [10] S. Tulin and H. -B. Yu, *Phys. Rep.*, **730**, 1 (2018).
  - [11] J. Magaña and T. Matos, *J. Phys.: Conf. Ser.* **378**, 012012 (2012).
  - [12] J. C. Niemeyer, *Progress in Particle and Nuclear Physics* **113**, 103787 (2020).
  - [13] E. G. M. Ferreira, *Astron. Astrophys. Rev.* **29**, 7 (2021).
  - [14] C. J. Pethick and H. Smith, *Bose-Einstein Condensation in Dilute Gases*, second edition, (Cambridge University Press, 2008).
  - [15] T. Matos and L. A. Ureña-López, *Phys. Rev. D* **63**, 063506(2001).
  - [16] C. M. González, J. E. M. Aguilar and L. M. R. Barrera, *Accelerated Cosmic Expansion : Proceedings of the Fourth International Meeting on Gravitation and Cosmology*, (Springer, 2013).
  - [17] M. P. Silverman and R. L. Mallett, *General relativity and Gravitation* **34**, 633 (2002).
  - [18] L. Hui, J.P. Ostriker, S. Tremaine, E. Witten, *Phys. Rev. D* **95**, 043541 (2017).
  - [19] D. J. E. Marsh, *Phys. Rep.*, **643**, 1 (2016).
  - [20] F. Dalfó, S. Giorgini, L. P. Pitaevskii, and S. Stringari, *Rev. Mod. Phys.* **71**, 463 (1999).
  - [21] A. L. Fetter, *Rev. Mod. Phys.* **81**, 647 (2009).
  - [22] M. C. Tsatsos, P. E. S. Tavares, A. Cidrim, A. R. Fritsch, M. A. Caracanhas, F. E. A. dos Santos, C. F. Barengi and V. S. Bagnato, *Phys. Rep.* **622**, 1 (2016).
  - [23] M. Tsubota, M. Kobayashi and H. Takeuchi, *Phys. Rep.* **522**, 191 (2013).
  - [24] L. Pitaevskii and S. Stringari, *Bose-Einstein Condensation*, (Oxford University Press, 2003).
  - [25] A. J. Leggett, *Quantum Liquids Bose Condensation and*

*Cooper Pairing in Condensed-Matter Systems*, (Oxford University Press 2006).

- [26] E. P. Gross, J. Math. Phys. Rev. **4**, 195 (1963).
- [27] L. P. Pitaevskii, Sov. Phys. JETP **13**, 451 (1961).
- [28] P. H. Chavanis, Phys. Rev. D **84**, 043531(2011).
- [29] P. H. Chavanis and L. Delfini, Phys. Rev. D **84**, 043532 (2011).
- [30] D. Harvey, R. Massey, T. Kitching, A. Taylor and E. Tittley, Science **347**, 1462 (2015).
- [31] M. Jauzac, D. Eckert, J. Schwinn, D. Harvey, C. M. Baugh, A. Rebertson, S. Bose, R. Massey, M. Owers, H. Ebeling, H. Y. Shan, E. Jullo, J. -P. Kneib, J. Richard, H. Atek, B. Clément, E. Egami, H. Israel, K. Knowles, M. Limousin, P. Natarajan, M. Rexroth, P. Taylor and C. Tchernin, Mon. Not. R. Astron. Soc. **463**, 3876 (2016).
- [32] C. G. Böhrer and T. Harko, JCAP **06**, 025(2007).
- [33] T. Harko, J. Cosmol. Astropart. Phys. **05**, 022 (2011).
- [34] T. Harko and F. S. N. Lobo, Phys. Rev. D **92**, 043011 (2015).
- [35] X. Zhang, M. H. Chan, T. Harko, S. -D. Liang and C. S. Leung, Eur. Phys. J. C **78**, 346 (2018).
- [36] B. Kain and H. Y. Ling, Phys. Rev. D **82**, 064042 (2010).
- [37] T. Rindler-Daller and P. R. Shapiro, MNRAS **422**, 135 (2012).
- [38] T. Harko, Phys. Rev. D **89**, 084040 (2014).
- [39] P.-H. Chavanis, Phys. Rev. D **94**, 083007 (2016).
- [40] P.-H. Chavanis, Phys. Rev. D **98**, 023009 (2018).
- [41] F. S. Guzmán, F. D. Lora-Clavijo, J. J. González-Avilés and F. J. Rivera-Paleo, J. Cosmol. Astropart. Phys. **09**, 034 (2013).
- [42] F. S. Guzmán and L. A. Ureña-López, Astrophys. J. **645**, 814 (2006).
- [43] F. S. Guzmán, F. D. Lora-Clavijo, J. J. González-Avilés and F. J. Rivera-Paleo, Phys. Rev. D **89**, 063507 (2014).
- [44] F. S. Guzmán, F. D. Lora-Clavijo, Gen. Relativ. Gravit. **47**, 21 (2015).
- [45] J. A. González and F. S. Guzmán, Phys. Rev. D **83**, 103513 (2011).
- [46] Y. O. Nikolaieva, A. O. Olashyn, Y. I. Kuriatnikov, S. I. Vilchinskii and A. I. Yakimenko, Low Temperature Physics **47**, 684 (2021).
- [47] A. S. Dmitriev, D. G. Levkov, A. G. Panin, E. K. Pushnaya and I. I. Tkachev, Phys. Rev. D **104**, 023504 (2021).
- [48] Y. O. Nikolaieva, Y. M. Bidasnyuk, K. Korshynska, E. V. Gorbar, J. Jia and A. I. Yakimenko, Phys. Rev. D **108**, 023503 (2023).
- [49] T. Harko, Eur. Phys. J. C **79**, 787 (2019).
- [50] J. M. Thijssen, *Computational Physics*, (Cambridge University Press, 2007).
- [51] Y. Nesterov, Soviet Math. Dokl. **27**, 372 (1983).
- [52] W. Su, S. Boyd and E. J. Candès, J. Mach. Learn. Res. **17**, 153 (2016).
- [53] B. O'Donoghue and E. J. Candès, Found. Comput. Math. **15**, 715 (2015).
- [54] Y. Castin and R. Dum, Phys. Rev. Lett. **77**, 5315 (1996).
- [55] K. Hayashi, M. Ibe, S. Kobayashi, Y. Nakayama and S. Shirai, Phys. Rev. D **103**, 023017 (2021).
- [56] D. S. Jin, J. R. Ensher, M. R. Matthews, C. E. Wieman and E. A. Cornell, Phys. Rev. Lett. **77**, 420 (1996).
- [57] M. -O. Mewes, M. R. Andrews, N. J. van Druten, D. M. Kurn, D. S. Durfee, C. G. Townsend and W. Ketterle, Phys. Rev. Lett. **77**, 988 (1996).
- [58] C. Deppner, W. Herr, M. Cornelius, P. Stromberger, T. Sterneke, C. Grzeschik, A. Grote, J. Rudolph, S. Herrmann, M. Krutzik, A. Wenzlawski, R. Corgier, E. Charon, D. Guéry-Odelin, N. Gaaloul, C. Lämmerzahl, A. Peters, P. Windpassinger and E. M. Rasel, Phys. Rev. Lett. **127**, 100401 (2021).
- [59] D. Lai, F. A. Rasio and S. L. Shapiro, ApJS, **88**, 205 (1993).
- [60] We introduce  $\tilde{\lambda}$  to maintain the values of the dimensionless variables within a range suitable for the numerical calculations.
- [61] These Euler-Lagrange equations suggest that the motion of the spherical self-gravitating BEC is analogous to that of the Friedmann model because Eq. (27) corresponds to the Friedmann equation. Here,  $R$  and  $H$  are the scale factor and the Hubble parameter, respectively.
- [62] In general, the gravitational energy of a spheroid is affected by its deformation (see [4]). However, we neglect these effects because, in the present study, we address only small oscillations.